Free-Space Optical Data Receivers with Avalanche Detectors for Satellite Downlinks Regarding Background Light

Dirk Giggenbach, 20220927

***Abstract*—Data Receiver Frontends using Avalanche Photodiodes are used in optical Free-Space Communications for their effective sensitivity, large detection area, and uncomplex operation. Precise control of the high-voltage necessary to trigger the avalanche effect inside the photodiode depend on the semiconductor's excess noise factor, temperature, received signal power, background light, but also the subsequent transimpedance amplifier's thermal noise behavior. Several prerequisites have to be regarded and are explained in this document. We focus on the application of avalanche photodiodes as data receivers for on/off-keying modulated bit streams with 50% duty cycle. Also, an experimental verification of the receiver performance with background light is demonstrated.**

***Index Terms*—Optical avalanche photo diode receiver frontend, RFE, InGaAs-APD, bias voltage control, temperature control, Q-factor, background light, Free-Space Optical Communication, FSO**

I. Introduction

AVALANCHE photo diodes (APD) detectors with Indium-Gallium-Arsenide semiconductor technology (InGaAs) together with low-noise transimpedance amplifiers (TIA) operating at 15xx nm wavelength are becoming the standard receiver-frontend (RFE) technology for optical inter-satellite links (as in mega-constellation satellite networks) as well as in space-to-ground communication [1]-[8]. APDs have been in use in low-cost fiber communication links up to 10 Gbps data rates, since their internal photo-electron gain allows for extended distance reach as compared to the ~10 dB less sensitive (and more conventional) positive-intrinsic-negative-photodiode (PIN) receiver technology [9]. While a constraint link-budget in fiber links can be compensated through intermediate optical amplifiers, this is not possible in long-range Free-space Optical Communications (FSO). Therefore, APD-RFEs are the preferred opto-electric frontend for optical space links with intensity-modulation and direct detection (IM/DD). Most relevant is simple On/Off-Keying (OOK) modulation, i.e. a digital 'one' is coded as a signal pulse. The foundations for such downlink technology were laid by the GEO-downlinks from OPALE onboard ESA's Artemis satellite in the SILEX-demonstration [10] and the OICETS-experiments in 2005 to 2009, that time still with silicon-based APDs operating at 8xx nm wavelength [10]-[13]. In current implementations, the wavelength range around 1550nm has evolved most useful due to re-use of terrestrial fiber-communication components (foremost efficient erbium-doped fiber amplifier, but also the range of wavelength channels, data-modulators and detectors). Also, the high achievable data rates and other methods for sensitivity increase (like optical pre-amplification or coherent modulation) are desirable. Optical space-communications here follows terrestrial fiber systems [14], but going through the atmosphere requires higher implementation effort. E.g. the adaptive optics for single-mode fiber coupling of an atmospherically distorted optical field [15]. Bulk APD-detectors do not require such sophisticated techniques and rather allow the focal illumination with an atmospherically distorted light field. This typically works up to 10Gbps and slightly more, where only for higher data rates the coupling into a single-mode fiber needs to be achieved. Besides pure communication, optical data transmission allows application of other photon-based techniques, like the exploitation of quantum effects for key-distribution transmission [16]. Current implementations of space-ground links employ component technology from Dense Wavelength Division Multiplexing (DWDM) with bulk optical detectors at the optical ground stations (OGS) [17]-[19].

A variety of environmental and orbital parameters influence the short- and long-term received optical power in long-range mobile FSO systems such as satellite up- and down-links [20]. Reasons for changes of mean received power – besides the blocking by cloud [21] - are the intermittent increase in atmospheric attenuation (haze, precipitation) [22], varying free-space loss (caused by changes in link-range), beam pointing errors [23], and scintillations caused by the atmosphere's index-of-refraction turbulence (IRT) [24]-[26]. Altogether, the mean received optical power can change by orders of magnitude in very short time frames. Sophisticated data electronic techniques - like adaptive coding and rate-adaptation - might be able to cover these steep and fast variations. However, also the physical APD-RFE parameters like diode bias voltage, limiter decider threshold, and receiver bandwidth must be constantly adopted to ensure optimum receiver performance. Specifically, the bias voltage is not only a function of temperature, but also of instantaneous received optical power, dark current, and foremost background-light as will be shown in section V [27]-[32]. The strength and velocity of such parameter variations in a typical low Earth orbit (LEO, ~500km circular orbit) to ground FSO scenario can be estimated as follows [33], [25]:

similar document has been published as: "Giggenbach, D. Free-Space Optical Data Receivers with Avalanche Detectors for Satellite Downlinks Regarding Background Light. Sensors 2022, 22, 6773. https://doi.org/10.3390/s22186773"

- Signal intensity changes due to distance variation by orbital movement from 5° elevation to zenith cause ~12dB variation.
- Additional signal power variation is introduced by increased atmospheric attenuation at low elevations, adding up to ~6dB of loss close to horizon, depending on OGS location.
- Background light at daytime and near to the horizon is stronger than at zenith by up to ~10dB. Variation-speed of these three effects is in few minutes, according to the LEO satellite's movement across the sky.
- Received-power scintillations (due to atmospheric IRT) typically adds another ~6dB or more, with timescales of milliseconds.
- Furthermore, the fast angular movement of a LEO-satellite across the sky (up to more than 1°/second) will lead to additional fading from dynamic pointing jitter.

In a controlled lab-environment, the performance of the data receiver can be determined by its required average energy-per-bit to achieve a given electrical signal quality. This is stated e.g. in SNR, Q-factor, or bit error ratio (BER). Overviews of practically achieved RFE sensitivities can be found in [34] p. 330 and in [35] Table III. Higher sensitivity has been reported by an alternative APD semiconductor material, HgCdTe, and commercial devices for FSO communication applications might soon be demonstrated [36] [37].
In a typical high-speed optical OOK receiver setup, the light-sensitive photodiode generates photo-electrons when illuminated by signal- or background-light photons. The photodiode is reverse-biased by U_R to control its operating point and possibly an internal electron-gain. The electrons are then converted into a voltage signal via transimpedance R_{TI}, filtered according to its required signal bandwidth, and binary decided by a limiting circuit (see figure 1).

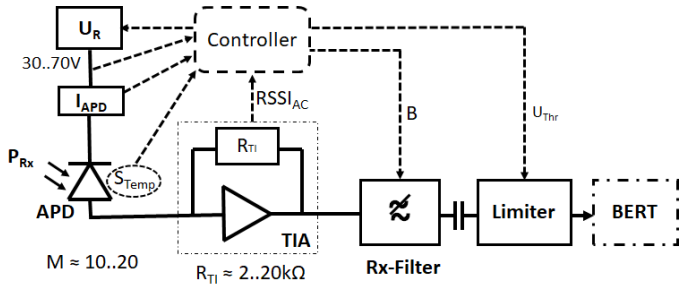

Fig. 1. Practical InGaAs-APD receiver for high-speed free-space optical (FSO) communications.

The variable U_R is adjusted according to APD-temperature (monitored by temperature sensor S_{Temp}), total APD-current as monitored by I_{APD}, optical received power P_{Rx} (must be monitored with an extra power sensor), and electrical signal amplitude as monitored via the received signal strength indicator (RSSI). The Rx-filter bandwidth B is adjusted to a 3db cutoff at roughly half the data rate r. To eliminate the influence of electronic offsets, AC-coupling is introduced before the limiter. The latter's threshold voltage U_{Thr} is also optimized via RSSI according to the asymmetric noise distributions of the APD-RFE. The system performance can finally be evaluated with means of a Bit Error Ratio Tester.
For an RFE with variable bandwidth / data rate it would be most beneficial in terms of sensitivity to adapt the feedback-resistance R_{TI} to the required bandwidth. However, this is not feasible with practical high-speed (>1Gbps) systems employing integrated circuits with a fixed feedback structure. Thus, the reduction of noise through the spectral filtering by the Rx-filter offers only a part of the possible SNR-optimization in a variable data rate RFE.

The remainder of this document is organized as follows: Section II summarizes basic relations of photodetectors and APD-performance modelling. Section III shows the dependency and optimization of the avalanche multiplication factor for CW illumination, and section IV describes theoretical RFE performance for On-Off-keying NRZ data modulation, with general sensitivity modelling between the two boundary cases - thermal- and shot-noise- limit. Section V introduces the influence of background light on receiver performance, where an analytical optimization for the multiplication factor is presented. A comparison with measurements from an exemplary APD-RFE is given. Section VI presents summary and conclusions. An addendum provides several helpful relations for RFE assessment.

II. Gain and Noise in Avalanche Photodiodes

In this section we consider the APD's sensitivity for an unmodulated - or continuous wave (CW) - optical signal illuminating the photo-sensitive detector area.
The received optical power P_{Rx} - in the form of photons impinging onto the detection area of a signal receiver - is exciting photo-electrons from the semiconductor's valence-band, via the detector material's responsivity R. This responsivity depends on signal wavelength λ and the semiconductor's conversion efficiency η. An additional multiplication gain M is achieved in APDs by an electric field inside the detection volume (caused by reverse-biasing of the diode), which accelerates the primary photo-electrons. These again strike out further (secondary) electrons in the multiplication region, causing an electron-avalanche. This way the signal current is increased by an internal multiplication factor of M:

$$I_{Sig} = M \cdot P_{Rx} \cdot R = M \cdot P_{Rx} \cdot \left(\eta \cdot \frac{q\lambda}{hc} \right) \qquad (1)$$

c = 2.998·10^8 m/s (speed of light in vacuum)
h = 6.626 10^{-34} Ws^2
q = 1.602 10^{-19} As
R Responsivity [A/W], for λ=1550nm is $R = \eta \cdot 1.250$ A/W
η quantum effic. of diode's detection region (typ. ~ 0.75 to 0.9)

The reception of a static power level is subject to variations of the photon-excited photoelectrons due to stochastic conversion

variations, and the variations of the photon-arrival probability itself. In APDs (as well as in most electron multiplication devices) the multiplication effect itself is subject to variations, resulting in additional noise effects. Expressions for the according distributions have been derived by McIntyre [38][39], confirmed experimentally by Conradi [40], and reviewed and simplified by Webb [41]. The signal-to-noise power ratio is derived for CW illumination with P_{Rx}, as the ratio of square of signal current I_{sig} to the sum of shot-noise and thermal-noise current variances (σ_s^2 and σ_t^2). Where we neglect the influence from level-offsets by background light and dark currents. The shot-noise variance σ_s^2 (in A^2) is calculated from currents I and the observation bandwidth B as $\sigma_S^2 = 2q \cdot I \cdot B$. And thermal noise density i_t (in $A/\sqrt{Hz}$) defines the thermal noise variance $\sigma_t^2 = i_t^2 \cdot B$. This allows to estimate the signal-to-noise power ratio as

$$\frac{S}{N} = \frac{I_{sig}^{\,2}}{\sigma_s^{\,2} + \sigma_t^{\,2}} = \\ = \frac{\left(P_{Rx} R M\right)^2}{B\left\{2q\left[I_{du} + \left(P_{Rx} R F_{sm} + \left(I_{dm} + R P_{BGL}\right) F_{dm}\right) M^2\right] + i_t^2\right\}} \tag{2}$$

With the APD's multiplication factor M, unmultiplied dark current component I_{du}, multiplied dark current component I_{dm}, responsivity of the detector material R, excess noise factor for signal current F_{sm}, excess noise factor for the multiplied dark current F_{dm}, and observation bandwidth B. I_{dm} is given through the biasing of the detector material itself, but is constant around the operating bias point U_{APD} - it will however generate a dark-current component, variable by its multiplication with M.

The thermal noise current density of the succeeding amplifier stage i_t can practically be found in data sheets, or is stated with a load resistor R_L, noise figure, and other constants (compare *Addendum B*). False background light power P_{BGL} can illuminate the detector and is added to the multiplied dark current. By making M large, the M^2-term in the denominator of (2) becomes larger than the thermal noise of the amplifiers, improving the SNR towards shot-noise limitedness. However, the APD's excess noise factor F_A will cause a local maximum here. We see that the performance of an APD is defined by its dark current, the excess noise factors, and an optimum M.

The excess noise factors are often simplified by equaling $F_A = F_{dm} = F_{sm}$, it quantifies the additional noise caused by the fluctuation of the avalanche multiplication process [41]:

$$F_A = \frac{\langle M^2 \rangle}{\langle M \rangle^2} \tag{3}$$

F_A depends on the ratio of the electron-hole generation $k_A = \alpha_h/\alpha_e$ in the specific APD-design and -material ($0 < k_A < 1$), by defining k_A as the smaller of the ratios of holes vs electrons. F_A has been derived as

$$F_A(M) = k_A \cdot M + 2(1 - k_A) + (k_A - 1)/M \tag{4}$$

For current InGaAs-APDs we find F_A typically ranging from 3 to 5 for M=10 and from 4 to 8 for M=20.

Different approximations have been suggested for (4) to allow further analytical evaluation of APD-performance [42]. The exponential approximation

$$F_A \approx M^{k_A^{0.355}} \tag{5}$$

models well for smaller M, and the exponent can be adopted to other ranges of M.

Furthermore, we find the linear approximation

$$F_A \approx 2 - 2k_A + k_A M \tag{6}$$

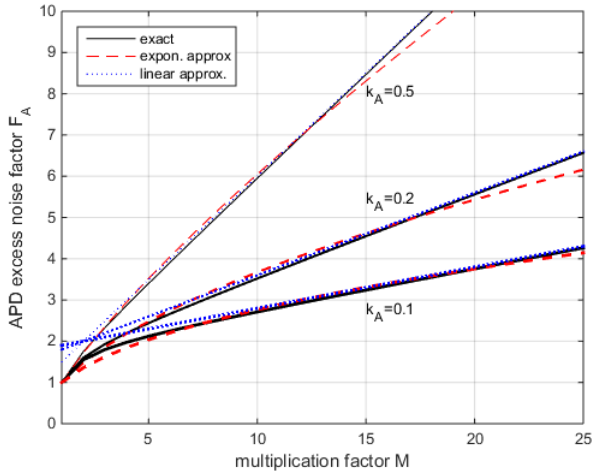

Fig. 2. Comparison of approximations (5) and (6) with exact solution (4)

From the comparison in Figure 2 we find that both approximations provide a good fit for $10 < M < 20$.

III. Optimum Multiplication for CW illumination

Depending on P_0, an optimum multiplication factor $M_{opt,CW}$ can be found in the CW-case by solving $d(SNR)/dM = 0$.

With the exact relation or also the linear approximation for F_A, further simplifications would be necessary to solve for $M_{opt,CW}$. However, with the exponential approximation (5) we can derive a closed-form solution for the optimum multiplication factor with CW-illumination:

$$M_{opt,CW} = \left(\frac{2q\, I_{dm} + i_t^{\,2}}{x \cdot q\, \left(R P_{Rx} + R P_{BGL} + I_{dm}\right)} \right)^{\frac{1}{2+x}} \tag{7}$$

with $x = k_A^{\,0.355}$

$M_{opt,CW}$ is a function of received power and further RFE parameters, but is independent of observation bandwidth B.

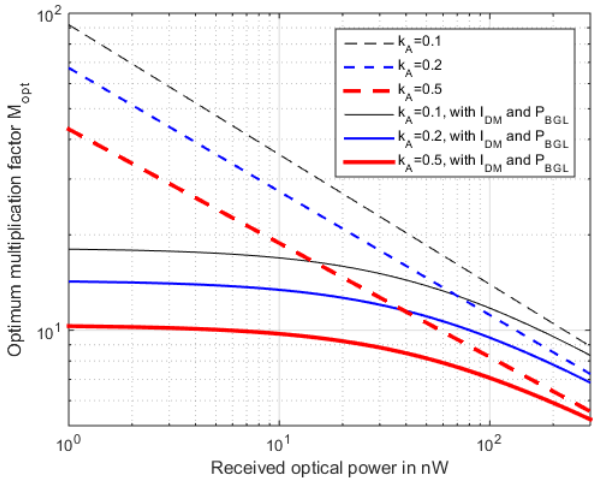

Fig. 3. Optimum multiplication factor M_{opt} with CW illumination, for different k_A, without and with I_{dm} =2.5nA and P_{BGL}=50nW.

For typical InGaAs-APDs and TIAs (using for i_t a typical 2.1pAHz$^{-0.5}$) we find $10<M_{Opt}<30$, see Figure 3.

We assume here that the excess noise factors for signal electrons and multiplied dark current electrons are equal, this assumption causes negligible error when the signal current is dominating the total avalanche current.

Dependency of M from bias voltage and temperature:

The electric field induced through the reverse voltage U_R causes the electron-hole avalanche, starting with M=1 at a minimum operating voltage (typical 1/3 of breakdown voltage U_{BD}). Beyond ~0.5·U_{BD} the multiplication increases according to (8) up to a pole at U_{BD} (see Fig. 4). When no BGL and no optical data signal is applied, only the APD's dark current is multiplied. In these conditions, U_{BD} is usually determined as the reverse voltage where the APD current exceeds 10µA.

The relation between bias voltage U_R and gain M is related in a simple rational term [42], [43]:

$$M(U_R) = \frac{1}{1-\left(\frac{U_R - I_{APD}\cdot R_S}{U_{BD}}\right)^n} \qquad (8)$$

The term $I_{APD}\cdot R_S$ in (8) indicates the voltage lost across the additional series resistance R_S of the photodiode (resistance of contacts and undepleted semiconductor region). This resistance is typically around 1 kΩ and the voltage-term thus is negligible for data communication. But it needs to be regarded in a situation with high optical power, especially since I_{APD} again is a function of the multiplication factor. Exponent n can be adopted to improved fitting to measured behavior, typically its value is slightly above one.

Figure 4 compares measured M of an InGaAs-APD-RFE (derived from RFE #7 of [35]) with the fit according to (8). For this type of APD U_R is typically 4% to 8% below breakthrough.

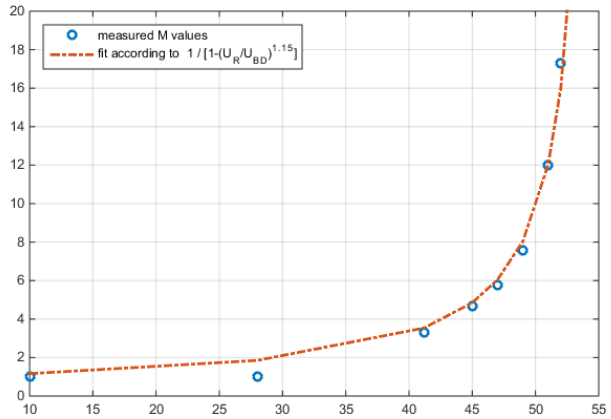

Figure 4. Measured and calculated M according to (8), over reverse voltage U_R for U_{BD}=55V and n=1.15

U_{BD} as well as U_R reduces along with temperature and can be approximated by a linear fit using temperature coefficient $\rho_T = \Delta U_R / \Delta T$ [44]

$$U_R = U_{R,ref} + \rho_T \cdot \left(T - T_{ref}\right) \qquad (9)$$

We find the required operating voltage U_R for a certain M by solving (8) with (9) (neglecting series resistance), as illustrated in Figure 5:

$$U_R = \left[U_{BD,ref} + \rho_T \cdot \left(T - T_{ref}\right)\right] \cdot \left(1 - \tfrac{1}{M}\right)^{\frac{1}{n}} \qquad (10)$$

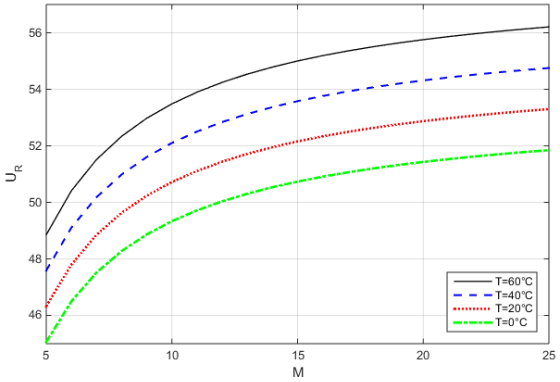

Figure 5: $U_R(M,T)$, for U_{BDref}=55V at 20°C, and ρ_T=0.075V/°C

We now can use the optimum M from (7) to describe the complete APD-voltage control loop at CW-illumination, including temperature compensation.

IV. Uncoded BER of APD OOK Receivers

We consider bit decision of an OOK data-stream with an APD-RFE including its noise processes. Figure 6 shows a

typical fraction of a pseudo-random bit sequence (PRBS) with 100Mbps data rate, detected with an APD-RFE. The shot-noise caused by the OOK-signal during reception of binary on-bits is obviously stronger than during zeros. Further information on Direct-Detection Receivers can be found in [45]-[52].

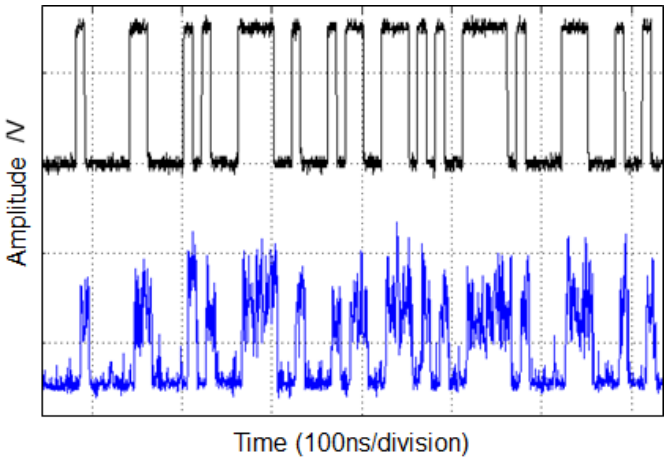

Figure 6: Typical binary OOK-data bit stream of 100Mbps as monitored on an oscilloscope: Upper plot transmitted data, lower plot is the received signal from an APD-RFE.

Noise is assumed gaussian distributed with different noise sigma at ones and zeros (figure 7). A detection threshold current level I_{Thr} between the curves around zeros and ones decides for binary 0 and 1. Decisions to the wrong side from I_{Thr} will lead to bit errors. Their probability is linear to the ratio of the stippled areas A+B related to the total curve-area.

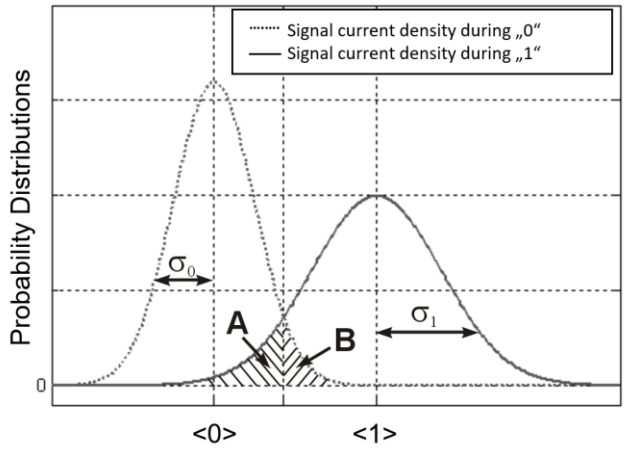

Fig. 7. Generic situation of the Gauss-shaped noise distributions at binary one and zero.

The areas on the wrong side of I_{Thr} are minimized with an optimum decision threshold level. For an analytically applicable approximation, I_{Thr} is defined by the intersection of both curves, which leads to …

$$I_{Thr} = \frac{\sigma_0 \cdot \langle s_1 \rangle + \sigma_1 \cdot \langle s_0 \rangle}{\sigma_0 + \sigma_1} \tag{11}$$

The quality factor Q can then be derived as

$$Q = \frac{\langle s_1 \rangle - \langle s_0 \rangle}{\sigma_1 + \sigma_0} \tag{12}$$

Assuming $\langle s_0 \rangle = 0$ (no offset), by integrating over the tails of the two gaussian distributions we get the bit error probability p_{BE}

$$p_{BE} = \frac{1}{2} \cdot erfc\left(\frac{1}{\sqrt{2}} \cdot \frac{\langle s_1 \rangle}{\sigma_0 + \sigma_1} \right) = \frac{1}{2} \cdot erfc\left(\frac{1}{\sqrt{2}} \cdot Q \right) \tag{13}$$

Where $\langle s_1 \rangle = M\, R\, \hat{P}_{Rx}$ is given by the optical power during an on-symbol, which is again twice the average power $\langle P_{Rx} \rangle$. Noise current during “0” and “1” consists of the same thermal noise current

$$\sigma_t = i_t \cdot \sqrt{B} \tag{14}$$

and the shot noise from background light and dark currents is

$$\sigma_{s,o} = \sqrt{B \cdot 2q\left[M^2 F_A \left(I_{dm} + R \cdot P_{BGL} \right) + I_{du} \right]} \tag{15}$$

Where during a binary “1” we see additional signal shot noise:

$$\sigma_{s,1} = \sqrt{B \cdot 2q\left\{ M^2 F_A \left[R \cdot \left(2\langle P_{Rx} \rangle \right) + I_{dm} + R \cdot P_{BGL} \right] + I_{du} \right\}} \tag{16}$$

Q then becomes

$$Q_{st,APD} = \frac{M\, R \cdot \left(2\langle P_{Rx} \rangle \right)}{\sqrt{{\sigma_{s,0}}^2 + {\sigma_t}^2} + \sqrt{{\sigma_{s,1}}^2 + {\sigma_t}^2}} \tag{17}$$

When neglecting the small unmultiplied dark current I_{du}, we find

$$Q_{st,APD} \approx \frac{M\, R \cdot \left(2\langle P_{Rx} \rangle \right)}{\sqrt{B} \cdot \sqrt{2qM^2 F_A \left(RP_{BGL} + I_{dm} \right) + {i_t}^2} + \ldots} \\ \overline{\ldots + \sqrt{B} \cdot \sqrt{2qM^2 F_A \left(R\left(2\langle P_{Rx} \rangle + P_{BGL} \right) + I_{dm} \right) + {i_t}^2}} \tag{18}$$

Sensitivity estimation without background light:

We find a general simplified (no P_{BGL}, no I_d) receiver sensitivity formula in terms of Q-factor, with signal power during the reception of a binary one $P_1 = 2\langle P_{Rx} \rangle$, and signal level during a binary zero is $P_0 = 0$. We regard the noise during binary zero and one ($\sigma_0 = \sigma_{thermal}$ and $\sigma_1 = \sqrt{{\sigma_{shot-1}}^2 + {\sigma_{thermal}}^2}$) and Photon-Energy $E_{Ph} = hc/\lambda$, and assume equal distribution of ones and zeros in the bit-stream:

$$Q_{APD} = \frac{M\,R\cdot\left(2\left\langle P_{Rx}\right\rangle\right)}{\sigma_t + \sqrt{\sigma_{shot-1}{}^2 + \sigma_t{}^2}} = \\ = \frac{\sqrt{8r}\cdot M\,R\cdot\left\langle N\right\rangle\cdot E_{Ph}}{i_n + \sqrt{4qM^2F_AR\cdot\left\langle N\right\rangle\cdot E_{Ph}\cdot r + i_n{}^2}} \qquad (19)$$

From Q we can derive p_{BE} via (13).
In one extreme, shot noise is negligible versus thermal noise, and the RFE operates purely in thermal-noise limit (*TNL*):

$$Q_{TNL} = \frac{R\cdot\left\langle P_{Rx}\right\rangle}{\sigma_t} = \frac{R\cdot\left\langle P_{Rx}\right\rangle}{i_t\cdot\sqrt{B}} = \frac{\sqrt{2r}\cdot R\cdot E_{Ph}}{i_t}\cdot\left\langle N\right\rangle \qquad (20)$$

Thus, Q is linear to $\langle N\rangle$, and to achieve a constant Q the bitwise sensitivity will decrease by $\sqrt{r}$, i.e. larger bandwidth shall be beneficial in terms of sensitivity. This relation however holds only as long as the receiver's amplifier is not adopted to B. But an adoption might be required to achieve a certain data rate, which at the same time means to choose the highest possible R_{TI}. Then again, the data-rate advantage of *TNL* practically will be compensated, compare figure 17.

In the other ideal extreme of shot-noise limit (*SNL*), multiplication M cancels, excess noise F_A becomes one, and thermal noise i_t is negligible vs the shot-noise:

$$Q_{SNL} = \frac{M\,R\cdot 2\left\langle P_{Rx}\right\rangle}{\sigma_{s,1}} = \sqrt{\frac{2R\cdot\left\langle N\right\rangle\cdot E_{Ph}}{q}} = \sqrt{2\eta\left\langle N\right\rangle} \qquad (21)$$

So in *SNL* the sensitivity in *Ppb* is independent from data rate, and the run of Q now corresponds linear to $\sqrt{\langle N\rangle}$ ([45] ch. 4.5.2).

Results here always assume gaussian noise distributions and presence of thermal noise also during a zero-bit. This theoretically is not true for an ideal photon-counting receiver without BGL or dark current, and becomes obvious when received number of photons is low: There will be no noise during zero thus the decision threshold will be close to zero, and furthermore the photon-arrival probability will be Poisson-distributed, not gaussian anymore [53]. The sensitivity numbers calculated with (20) and (21) therefore deviate from ideal Poisson statistics, when the Ppb becomes very low. In our regime of dozens of photons per one-bit, however, the preceding formulas provide a sufficiently accurate approximation.

The above findings can be compared on logarithmic scales for received-power as shown in figures 8 through 10, employing real-world APD parameters from table III. In figures 8 and 9 the data rate is varied while the TIA's noise density stays constant – thus only the reception filter is adopted to data rate. We find that *M=25* is an advantageous *fixed* value for 1 Gbps, when no I_D or P_{BGL} are present (compare Figure 11), which is however only an idealized case.

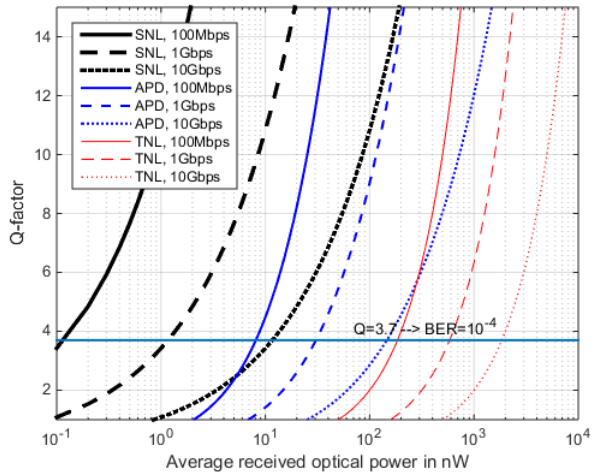

Figure 8: RFE-sensitivity for the three RFE-cases with M=25. The RFE here has constant TIA-noise density but an adoptive Rx-lowpass.

The sensitivity-runs of the different RFE-types become steeper, from SNL via APD to TNL, and typically a 10dB sensitivity step is seen for same BER in between these technologies (Figure 8, compare plots of same line-style). However, going from PIN to APD is only a moderate technology step, while building and operating a SNL (photon counting) receiver at 15xx nm wavelength requires much higher complexity and expenditure [54]. Figure 9 plots the BER-sensitivity in photons per bit, for a fixed M=25 and a TIA covering rates up to 10Gbps. Since the TI-amplifier's noise density is assumed constant here (2.1pA/sqrt(Hz) for all data rates), and only the bandwidth of the separate reception filter is adopted to data-rate, the sensitivity is rate-dependent.

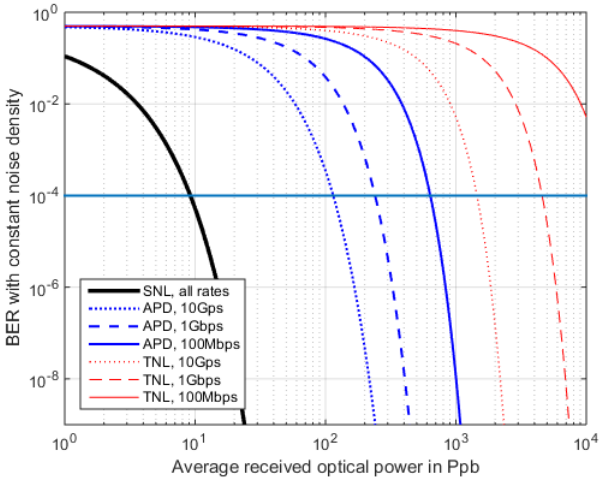

Figure 9: BER from <N>, with constant TIA noise-density and adaption of receiver-filter only. Same parametrization as figure 8.

This assumption however is unpractical for many systems, since selection of the TIA-component then would depend on the highest employed bandwidth (here 10 Gbps) - that would mean unnecessary high noise density values for the lower rates (1 Gbps or 100 Mbps). In other words, the TIA's noise density in a data rate-optimized RFE-setup must follow its bandwidth. As a simple explanation for this behavior: the amplification of

the TIA can be chosen higher to offer a better SNR, but at the same time the bandwidth is reduced through $1/R_{TI}$.
So, in another setup one adopts the bandwidth of the TIA (and thus its R_{TI}) with the sqrt(B)-characteristic of the current noise density i_n, as shown in Fig. 17, and in Table II for 500MHz bandwidth. For data rates 100Mbps / 1 Gbps / 10Gbps the noise densities are 0.66pA·Hz$^{-0.5}$ / 2.1pA·Hz$^{-0.5}$ / 6.6pA·Hz$^{-0.5}$ accordingly. This results in TIA-adopted sensitivity for TNL and partly in APD, leading again to all sensitivity-runs independent from r since in the calculation of Q both noise-bandwidth adoption methods will then cancel with the increase in received signal power (solid lines in figure 10). When adding a fixed I_{dm}=2.5nA however (dashed lines in figure 10), its changing ratio versus the received power will again lead to r-dependency, and we see a strong performance degradation specifically with SNL due to false detection of electrons from I_{DM}. For *TNL* however the plot with I_{dm} is too close to the original curve to be distinguished (red line(s)).

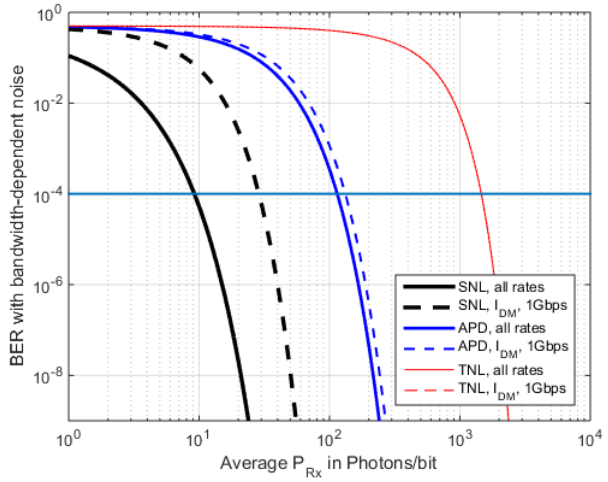

Figure 10: BER from Ppb, for a sqrt(B)-dependent TIA noise density according to data rate, plus adaptation of reception-filter bandwidth. Sensitivity curves with I_{dm} are shown for comparison (for 1Gbps, no BGL).

In practical systems we might see both RFE characteristics: When both, B and the R_{TI}, can be optimized to one fixed r, the sensitivity is improved and then also constant in Ppb (fig. 10). When, however, in a variable-rate system only the bandwidth of the Rx-filter can be adopted to r, overall sensitivity will reduce with decreasing B when thermal noise is present, as shown in figure 9.

V. Optimum *M* with Background Light

Power of Background Light:

In an FSO-Receiver, background light from the sun or sunlight reflected by celestial bodies or clouds / air / ground-structures, is a significant source of noise and electronic offset in detectors. BGL-induced current flowing through the APD will add extra shot-noise, just as the detector's dark current does.
Values of P_{BGL} depend on receiver aperture size, Field-of-View (FoV) angle of the detector, optical bandwidth of background blocking filters, and spectral behavior of the background source itself which also implies the wavelength (e.g. blue-sky and haze at certain elevation, sunlit clouds, spectral luminance of background structure behind a data source) [28]-[32]. These environmental parameters can be summarized by the spectral irradiance $L_{e,\Omega,\lambda}$ in [$W/m^2/nm/sr$]. We state here only some typical figures with the sun far above horizon, to allow a rough estimation of P_{BGL}, where detailed analysis would be required for precise values in individual scenarios, more precisely the angle of Sun-Earth-Target and the Sun-elevation would have to be considered.

Table I: BGL Spectral Irradiance at Different Wavelengths

$W / (m^2\ nm\ sr)$	λ = 850 nm	λ = 1064 nm	λ = 1550 nm
on Sun-disk	20 E+3	10 E+3	2 E+3
blue sky zenith	2.0 E-3	2.3 E-3	1.2 E-3
blue sky 30° el.	3.5 E-3	4.0 E-3	2.0 E-3
blue sky horizon	30 E-3	30 E-3	25 E-3
sunlit cloud	200 E-3	80 E-3	20 E-3
overcast cloud	20 E-3	8 E-3	2 E-3
on Moon-disk	400 E-3	220 E-3	20 E-3
full Mars-disk	11 E-12	8 E-12	3 E-12

Small celestial bodies (like planets or stars) exhibit a very limited apparent size which normally falls far below the detector's FoV. On the other side, looking at the sun must be absolutely avoided.

$$P_{BGL} = L_{e,\Omega,\lambda} \cdot A \cdot \Omega \cdot \Delta\lambda \qquad (22)$$

with the receiver-telescope aperture area A in m^2, the optical filter bandwidth $\Delta\lambda$ in nm, and the detector's solid angle FoV Ω, which is derived from the more common full-flat-angle ω: $\Omega = 4\pi\ sin^2\omega$
With typical OGS geometries and for 1550nm signal wavelength, we find the following exemplary values of background light:

Table II: Typical values of P_{BGL} at 1550nm wavelength

Scene	$L_{e,\Omega,\lambda}$ in $W / (m^2\ nm\ sr)$	A in m^2	ω in μrad	$\Delta\lambda$ in nm	P_{BGL} in nW
towards horizon	25E-3	0.1	200	40	50
towards horizon	25E-3	0.7	100	40	88
to zenith	1.2E-3	0.1	200	40	2.4
to zenith	1.2E-3	0.7	100	40	4.2

Where 0.1m^2 refers approx. to a Cassegrain-telescope with 40cm aperture diameter, and 0.7m^2 to a 1m telescope. A 40nm wide filter covers the whole C-Band and thus supports the span of several DWDM channels.

We find 88 nW a large value for P_{BGL} from horizon-sky at daytime (and a similar value when looking onto the sun-illuminated Moon disk), while 2.4 nW serves as a minimum value. At night time of course BGL should be negligible (except when celestial bodies are in the FoV). For further examples, we chose 50 nW as a typical strong BGL value.

Optimum Multiplication Factor with BGL:

From above analysis we compare the BER over M, without and with BGL.

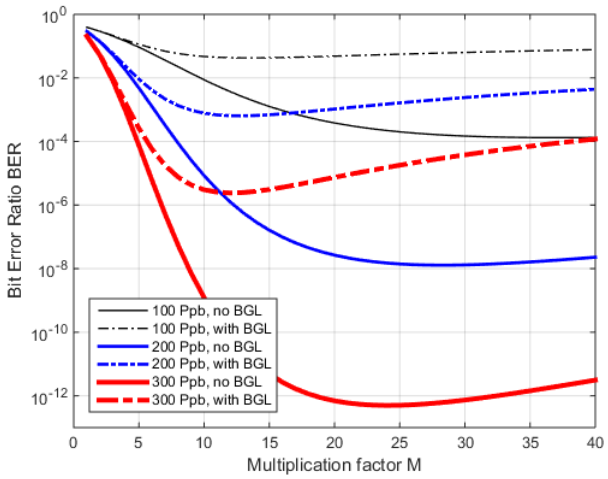

Fig. 11. Dependency of BER against M, without and with BGL (P_{BGL}=50nW), and three received signal levels for 1Gbps.

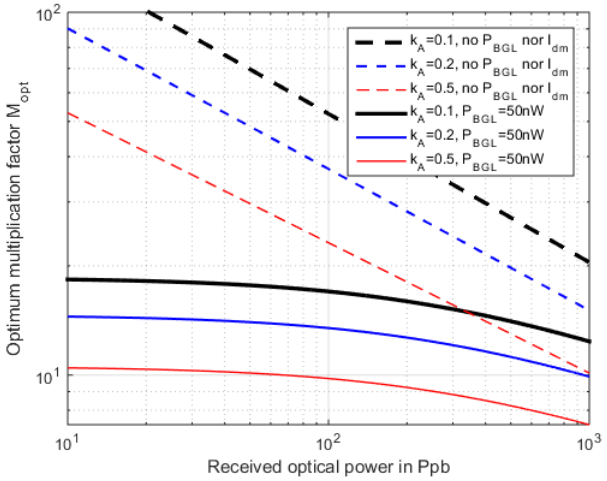

Fig. 12. Optimum multiplication factor M_{opt} with NRZ-50:50 modulated signal, for different ionization ratios, according to (24).

The optimum multiplication factor in the examples of Figure 11 varies from ~10 to ~40, and a wrong value can reduce the BER by orders of magnitude. As an example, with 50 nW of BGL and 200 Ppb the M_{opt} is 12, while without BGL M_{opt} is 28. Then, when using the M_{opt} for BGL without this BGL, the BER would increase from 10^{-8} (at $M=28$) to 10^{-6}. Controlling M dependent on the varying $<P_{Rx}>$ and BGL, therefore, is a must in optimized FSO-APD-receivers.

As with (7), we can derive from (18) a formula for the optimum M to achieve maximum Q in APD data receivers, with the exponential approximation of F_A, and with NRZ modulation, now again regarding I_{dm} and BGL:

$$\frac{dQ}{dM}=0 \rightarrow d\left(\frac{M}{\sqrt{M^{2+x}A+B}+\sqrt{M^{2+x}(A+C)+B}}\right)/dM=0 \qquad (23)$$

$$with\ A=2q\left(RP_{BGL}+I_{dm}\right);\ B=i_t{}^2;\ C=2qR\cdot 2\left\langle P_{Rx}\right\rangle;\ x=\ k_A{}^{0.355}$$

In contrast to the term with CW illumination, the derivation here results in:

$$M_{opt}=\left(\frac{-b+\sqrt{b^2-4ac}}{2a}\right)^{\frac{1}{2+x}} \qquad (24)$$

with

$$a=x^2AC(A+C)$$
$$b=x^2BC(2A+C)$$
$$c=-4(x+1)B^2C$$

As shown in Figure 12 for different k_A, M_{opt} with data modulation differs significantly from CW illumination (compare figure 3).

The relation in Chapter 4.5.2 of [45], and in [46], also describes a relation for the optimum M, however requiring numerical evaluation.

For the following comparisons we assume the values from table II with 1Gbps data rate. The optimization of M is independent from data rate (only requires the fraction of on-time vs off-time to be 50:50), but depends on received signal power $<P_{Rx}>$. When regarding bit-length, however, we can relate this received power to energy per bit.

With the optimization of M from (23), (24) we understand the importance of adjusting M to the received power especially in the low-power / high-BER regime. Figure 13 shows the effect of optimized versus fixed M on BER, with and without background light and dark current.

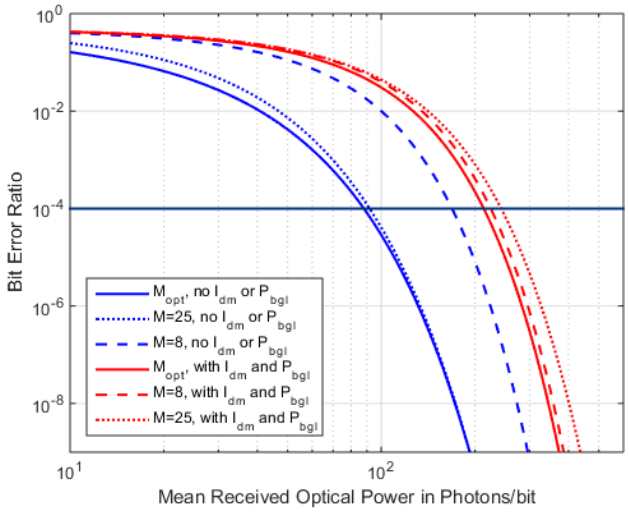

Fig. 13: BER over <N>, with fixed M=8 and M=25 compared with M_{opt} adopted to P_{Rx}, without and with P_{BGL}=50nW and I_{dm}=2.5nA.

A fixed and high *M of 25* offers comparable performance like the optimized M when no BGL and no I_{dm} are present, while a low *M of 8* shows inferior sensitivity. But the same fixed high M will provide less sensitivity when such additional shot noise sources are present, and the low M then nearly coincides with the optimized M. In any case, the curves are much closer to each other when additional shot-noise is present.

Methods to optimize M automatically for varying input power have been suggested for fiber communications [55]. Such however are of marginal applicability in the case of FSO with its large and variable fraction of background light, and with an even faster varying received power (due to scintillation and pointing-fading). Rather, a BGL-sensor would need to be added and evaluated, to ensure minimum p_{BE} in any situation. Thus, when BGL and I_{dm} can be measured and are not negligible, it is important to ensure the advantageous fixed multiplication factor for the individual environmental situation. Figure 14 signifies its importance by plotting BER and the M_{opt} for a range of BGL and three values of $<P_{Rx}>$ (no I_{dm} regarded here for better comparability).

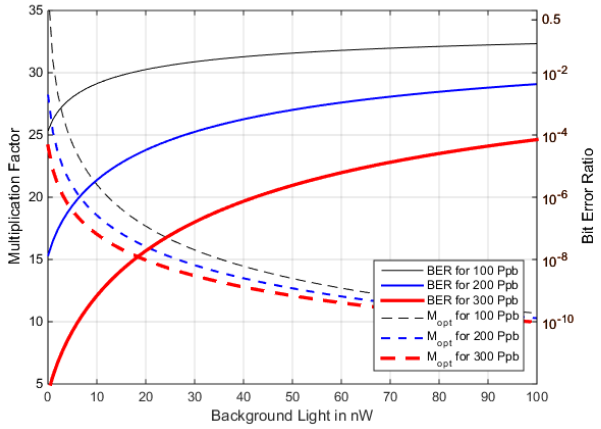

Fig. 14: BER and M_{opt} over P_{BGL}, at P_{Rx} of 100/200/300 Ppb, for BGL from 0 to 100nW (no I_{dm} to visualize the effect of BGL-only)

We find that the multiplication factor M_{opt} requires careful adoption to the instantaneous background light to ensure optimum performance of the APD-RFE, while the influence of absolute received power on M_{opt} is less significant in this example since its shot-noise component is small compared to BGL. The more background light the less important is individual optimization of M, tending towards a value around 8 with the parametrization used here.

The foregoing findings are verified by measurements with a free-space APD-RFE-implementation, with and without the influence of a 1550nm BGL source (Figure 15).

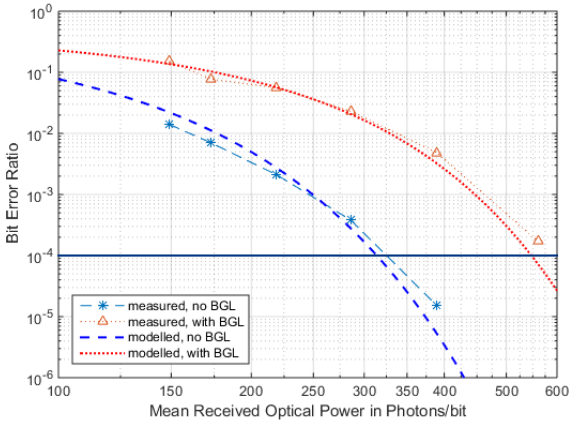

Fig. 15: Measured BER-performance with and without BGL, for M_{opt} (i_n=2.5pA/Hz^5, I_{dm}=9nW, P_{BGL}=50nW, B=500MHz, r=300Mbps)

The practical RFE used here shows some real-world deteriorations: the bandwidth of TIA, reception-lowpass (LP), and limiter do not match, and the high capacitance of the large APD (200 µm in diameter) again limits its usable data rate and thus its sensitivity. These lead to 320Ppb at BER=10^{-4} instead of the ideal ~120Ppb. The measured sensitivity-run and the effect of background light coincide well with the predictions from the formalism presented in this section: The deterioration of sensitivity of nearly -3dB at BER=10^{-4} between with and without BGL is confirmed.

VI. Summary and Conclusion

In this document we summarize basic relations of free-space APD receivers with emphasize on optical LEO data downlinks including background light. Such data reception is prone to fast and strong signal- and background-light variations due to atmospheric and mechanical effects. Furthermore, changes in atmospheric attenuation and strength of background light with elevation adds to this dynamic parametrization. We derive a model for the optimum multiplication factor in (23) and (24) and evaluate its relation to signal power, background light, and other parameters, embracing its performance in (18).

We find that the dependence of the optimum multiplication factor from background light and data signal strength suggests to measure both parameters. According control of the APD biasing-voltage U_R is recommended to ensure the optimum receiver performance in all FSO situations - additionally to its dependency from temperature. With a high amount of background, the optimization of the multiplication becomes less important, and rather a fixed value can be used.

The RFE-performance will also suffer from other effects like non-matching bandwidths of TIA, reception-filter, and limiter, and from noise effects through limited stability of the biasing voltage.

One of the parameters that can practically be controlled is the limitation of background light through narrow chromatic filtering, however, the data signal's channels width (spectral broadness of data signal) sets a limit to this reduction. Furthermore, the receiver telescope's FoV can be reduced by opto-mechanic measures, then requiring but more precise pointing and tracking of the signal source during communication. Other parameters lie by the sophistication of the APD itself, namely the tapering of dark current and excess noise factor.

Acknowledgements

The author wants to thank M. Knopp and F. Lippert for discussions and their assistance with measurements. This research was partly supported by the DLR Responsive Space Cluster Competence Center (RSC^3) on behalf of the German Federal Ministry of Defense (BMVg).

similar document has been published as: "Giggenbach, D. Free-Space Optical Data Receivers with Avalanche Detectors for Satellite Downlinks Regarding Background Light. Sensors 2022, 22, 6773. https://doi.org/10.3390/s22186773"

TABLE III: TYPICAL VALUES FOR A 1 GBPS APD RFE

Quantity	Symbol	Value
detector diameter	D	200 µm
APD capacitance	C	1.7 pF
Quantum efficiency at 1550nm	η	0.8
Responsivity at 1550nm	R	1 A/W
dark current (to get multiplied with M)	I_{dm}	2.5 nA
APD bandwidth	B_{APD}	800 MHz
hole-electron ionization ratio	k_A	0.2
Excess noise Factor for M = 10 / 20	F_A	3.5 / 5.6
temperature coefficient of U_{BD}	ρT	+0.075 V/°C
breakdown voltage	U_{br}	65 V
typical constant M, for a superior InGaAs-APD (no BGL and no I_{DM})	M_{typ}	25
TIA full bandwidth	B_{TIA}	580 MHz
TIA input-referred noise density in 580MHz	i_n	2.1 pA/sqrt(Hz)
TIA input-ref. RMS noise in ~500MHz	$<I_n>$	47 nA
Transimpedance resistance	R_{TI}	18 kΩ
background light power range, typical	P_{BGL}	2.4 .. 80 nW
bandwidth of electronic reception filter	B	500 MHz
data rate	r	1.0 Gbps

Values partly based on IAG200X [56] and MAX3658 [57]

ADDENDUM: GENERAL CONSIDERATIONS IN RFE DESIGN

A. *Photon Density in a Binary Optical OOK Signal*

Energy of one photon is calculated by $E_{Ph} = hc/\lambda$, and the average number of photons per bit (Ppb) $\langle N \rangle$ in a binary data stream (with rate r $[bit/s]$ and average power $\langle P_{Rx} \rangle$) is thus $\langle N \rangle = \langle P_{Rx} \rangle \cdot \lambda / (hcr)$.

Assuming IM/DD of OOK with 50% mark-zero ratio, there is twice the power in an on-bit than in the whole data stream on average, i.e. $\widehat{P_1} = 2 \cdot \langle P_{Rx} \rangle$. Sensitivity in photons per bit as well as the signal power are always stated for the *average* power value in this document. Figure 16 signifies the relation from mean Photons-per-Bit to average received power, for three different data rates.

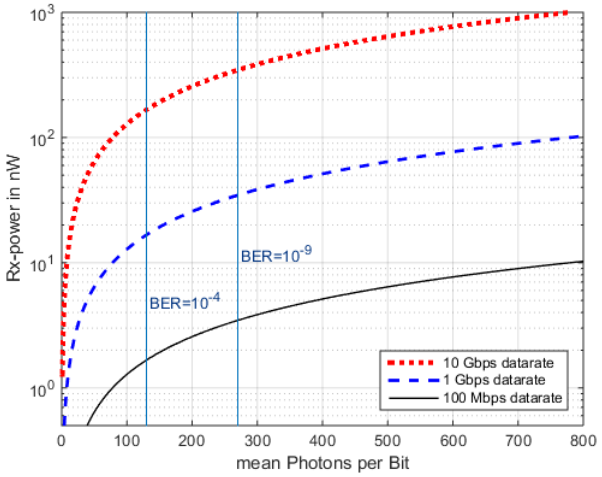

Fig. 16: Reference of P_{Rx} vs Ppb for different data rates, at 1550nm wavelength, with BER-lines as for an ideal constant-Ppb RFE.

B. *Thermal Noise of Transimpedance Amplifiers*

Signal current from the photodiode is converted into voltage by a transimpedance amplifier TIA over feedback resistor R_{TI}. The inherent thermal noise of this TIA together with the APD's F_A defines the sensitivity of the RFE.

Amplifier noise power is classically modeled by a thermal gaussian noise process over a resistor R_L times an additional deteriorating amplifier noise figure F_n ([45] p157):

$$\sigma_t^2 = \left(4k_B T / R_L\right) F_n B \tag{25}$$

with absolute temperature T, Boltzmann constant k_B and physical (one-sided) bandwidth B.

This formula shows the dependence of noise current σ_T with $\sqrt{B}$. With today's common use of integrated high-speed TIA circuits it is however more practical to relate this formula to the input-referred current noise density i_n in A/sqrt(Hz), as stated in data sheets:

$$\sigma_t = i_n \sqrt{B} \tag{26}$$

Setting R_L=R_{TIA} allows relating σ_T to the noise figure:

$$F_n = \frac{i_n^2 R_{TIA}}{4k_B T} \tag{27}$$

A comparison of TIA noise density values from data sheets is given in figure 17, where roughly a $B^{0.5}$-increase of current noise density can be observed. The exact dependence of noise density and TIA-bandwidth is subject to several component specific parameters like semiconductor technology, control of stray capacitance and optimization of amplifier-peaking versus its gain-bandwidth product, etc.

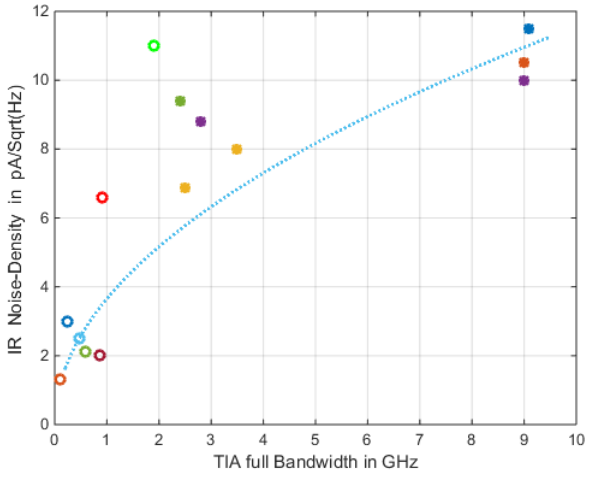

Fig. 17. Input-referred current noise densities of several commercial transimpedance amplifiers, from data sheets. Circles represent housed ICs while filled dots are for bonded dies. Dotted blue trend line follows $B^{0.5}$.

C. *Q related to BER*

The quality factor Q in OOK-receivers equals $SNR^{½}$.

$$p_{BE} = \frac{1}{2} \cdot erfc\left(\frac{Q}{\sqrt{2}}\right) = \frac{1}{2} \cdot erfc\left(\sqrt{\frac{SNR_{el}}{2}}\right) \quad (28)$$

Figure 18 visualizes the steep decrease of P_{BE} with moderate values of Q, including also the useful approximation ([42] ch.4.5.1.)

$$p_{BE} \approx \frac{e^{-\frac{Q^2}{2}}}{Q \cdot \sqrt{2\pi}} \quad (29)$$

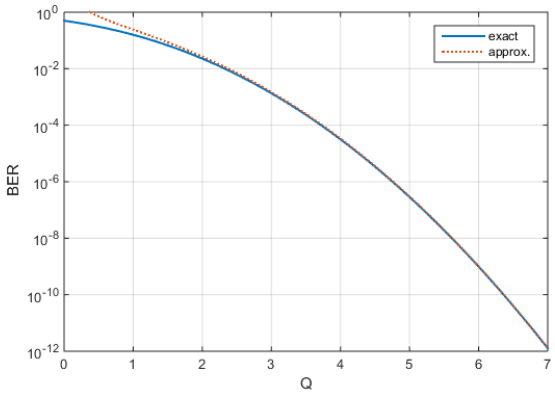

Fig. 18. Relation of Q-factor and p_{BE} according to (28).

TABLE IV: RELATIONS BETWEEN Q AND BER IN OOK-SYSTEMS

Q	SNR_{el}	p_{BE}
0	0	0.5
1	1	0.16
2	4	0.023
2.3	5.4	$1.0 \cdot 10^{-2}$
3.1	9	$1.0 \cdot 10^{-3}$
3.7	14	$1.0 \cdot 10^{-4}$
4.8	23	$1.0 \cdot 10^{-6}$
6	36	$1.0 \cdot 10^{-9}$
7	49	$1.3 \cdot 10^{-12}$

D. RFE-Bandwidth

The usable bandwidth - or applicable data rate $r=2B$ - of an RFE is defined by the APD-bandwidth, the TIA-APD-combination, the LP, and the limiter. Since only the LP shall dominate B, the other components must be chosen not to conflict with this requirement. This is however partly contradictive, since often the APD-size shall be as large as possible to ease optical spot requirements, as well as the TIA shall bear highest possible transimpedance to exhibit lowest noise-density, while both requirements this limits bandwidth. The following summarizes some rules for optimization of the signal processing chain:

Manufacturers often state a bandwidth for their photodiodes, although this would require further data of its implementation [58]. However, for an appraisal of bandwidth potential, the photodetector's capacitance (as well as the multiplied dark current) can be assumed linear to its area, leading to the following rough estimation for typical InGaAs-APDs, based on bandwidth values from APD data sheets (D_{APD} is detector diameter):

$$B_{APD} \approx 40\ Hz \cdot m^2 / D_{APD}^2 \quad (30)$$

The usable bandwidth of the combination of APD and TIA will be further limited by input capacitance to the TIA (the APD's capacitance plus further capacitance from TIA and the signal traces on the circuit board. The TIA's data sheet might state the expected bandwidth under certain input capacitance assumptions. Since this capacitance is mainly given through the APD's *size*, its diameter reduction – if applicable - might increase B of the RFE significantly.

Further the limiter shall exhibit high sensitivity to the signal level from TIA and LP, but still support a high r. Again, both parameters limit each other, requiring according optimization.

ACRONYMS AND SYMBOLS

APD	Avalanche Photo Diode (or ~Detector)
BERT	Bit Error Ratio Tester
BGL	Background Light
FoV	Field-of-View
InGaAs	Indium Gallium Arsenide semiconductor
IM/DD	Intensity Modulation / Direct Detection
IRT	Index-of-Refraction Turbulence
LEO	Low Earth Orbit
LP	Low Pass, or reception filter (between TIA and limiter)
OOK	On/Off-Keying modulation
PRBS	Pseudo-Random Bit Sequence
Ppb	Photons per symbol-bit
RFE	Receiver Front-End
RSSI	Received Signal Strength Indicator
SNL	Shot-Noise Limited
SNR	Signal-to-Noise Ratio
TIA	Trans-Impedance Amplifier
TNL	Thermal-Noise Limited
B	bandwidth, e.g. of the RFE's reception filter
c	speed of light in vacuum ($2.998 \cdot 10^8$ m/s)
F_A	excess noise factor of an APD
F_n	amplifier noise figure
h	Planck constant ($6.626\ 10^{-34}$ Ws^2)
i_t	thermal noise current density from amplifier
I_d	dark current of a photodiode
I_{dm}	part of dark current that will get multiplied with M
I_{du}	part of dark current that will not get multiplied
k_A	ionization-coefficient ratio of electrons-vs-holes
k_B	Boltzmann-constant
$L_{e,\Omega,\lambda}$	spectral irradiance (typically per nm wavelength)
M	Multiplication factor
M_{opt}	optimum multiplication factor
$\langle N \rangle$	mean number of photons per bit
$\langle P_{Rx} \rangle$	mean received optical power
P_{BGL}	background light power seen by the APD-area
p_{BE}	probability of bit error
Q	receiver Quality-factor
q	elementary charge ($1.6022\ 10^{-19}$ As)
R	unmultiplied detector Responsivity
R_{TI}	Transimpedance-Resistor
r	data-rate = ½ B
T	temperature
U_{BD}	breakdown voltage of APD
U_R	reverse voltage applied to APD
$\hat{..}$	peak signal value (e.g. pulse-amplitude)
$\langle .. \rangle$	mean value of a binary symbol sequence

REFERENCES

[1] B. L. Edwards, “Latest Status of the CCSDS Optical Communications Working Group”, 2022 IEEE International Conference on Space Optical Systems and Applications (ICSOS), Kyoto, Japan, 2022

[2] “OPTICAL COMMUNICATIONS PHYSICAL LAYER RECOMMENDED STANDARD”, CCSDS 141.0-B, Consultative Committee for Space Data Systems, 2021

[3] D. Giggenbach, “Standards for Optical Space Communication Satellite and Space Communications”, IEEE-SCC Newsletter, Vol. 30, December 2020

[4] I. del Portillo, B. G. Cameron, E. F. Crawley, “A Technical Comparison of Three Low Earth Orbit Satellite Constellation Systems to Provide Global Broadband”, Acta Astronautica Vol. 159, June 2019

[5] A. U. Chaudhry, H. Yanikomeroglu, “Laser Intersatellite Links in a Starlink Constellation – A Classification and Analysis”, IEEE Vehicular Technology Magazine, p 48-56, June 2021

[6] H. Henniger, O. Wilfert, “An Introduction to Free-space Optical Communications”, Radioengineering, 2010 Vol. 19, No. p. 203-212

[7] D. Giggenbach, F. Moll, C. Schmidt, C. Fuchs, A. Shrestha, “Optical on-off keying data links for low Earth orbit downlink applications”. Satellite Communications in the 5G Era, IET TELECOMMUNICATIONS SERIES, 79, 2018

[8] H. Kaushal, G. Kaddoum, “Optical Communication in Space: Challenges and Mitigation Techniques”, IEEE COMMUNICATIONS SURVEYS & TUTORIALS, VOL. 19, NO. 1, 2017

[9] O. Kharraz, D. Forsyth, "Performance comparisons between PIN and APD photodetectors for use in optical communication systems", Optik, Volume 124, Issue 13, 2013

[10] J. Romba, Z. Sodnik, M. Reyes, A. Alonso, A. Bird, "ESA's bidirectional space-to-ground laser communication experiments," Proc. SPIE 5550, Free-Space Laser Communications IV, 20 October 2004

[11] N. Perlot, et al, „Results of the Optical Downlink Experiment KIODO from OICETS Satellite to Optical Ground Station Oberpfaffenhofen (OGS-OP)”, Proc. of the SPIE -- Volume 6457, 2007

[12] T. Jono, Y. Takayama, N. Perlot, D. Giggenbach, et al, “Report on DLR-JAXA Joint Experiment: The Kirari Optical Downlink to Oberpfaffenhofen (KIODO)”, JAXA and DLR, ISSN 1349-1121, 2007

[13] D. Giggenbach, F. Moll and N. Perlot, “Optical communication experiments at DLR", NICT Journal Special Issue on the Optical Interorbit Communications Engineering Test Satellite (OICETS), 59, 2012

[14] M. Knopp, A. Spörl, M. Gnat, et al, “Towards the utilization of optical ground-to-space links for low earth orbiting spacecraft”, Acta Astronautica (166), Elsevier, ISSN 0094-5765, 2019

[15] E. Fischer, et al, "Use of adaptive optics in ground stations for high data rate satellite-to-ground links", ICSO 2016 - International Conference on Space Optics, 2016

[16] A. Carrasco-Casado, H. Takenaka, D. Kolev, et al, “LEO-to-ground optical communications using SOTA (Small Optical TrAnsponder) – Payload verification results and experiments on space quantum communications”, Acta Astronautica, Vol. 139, 2017

[17] C. Fuchs, F. Moll, D. Giggenbach, C. Schmidt, J. Keim, S. Gaisser, “OSIRISv1 on Flying Laptop: Measurement Results and Outlook”, 2019 IEEE International Conference on Space Optical Systems and Applications, ICSOS 2019. IEEE International Conference on Space Optical Systems and Applications, Portland, Oregon, USA, 2019

[18] J. Keim, S. Gaißer, P. Hagel, et al, “Commissioning of the Optical Communication Downlink System OSIRISv1 on the University Small Satellite Flying Laptop”, 70th International Astronautical Congress (IAC), Washington, 2019

[19] F. Moll, A. Shrestha, C. Fuchs, “Ground stations for aeronautical and space laser communications at German Aerospace Center”, Proc. of SPIE 9647, 2015

[20] D. Giggenbach, F. Moll, C. Fuchs, T. de Cola, R. Mata-Calvo, "Space Communications Protocols for Future Optical Satellite-Downlinks", 62nd International Astronautical Congress, Cape Town, South Africa, 2011

[21] C. Fuchs, S. Poulenard, N. Perlot, J. Riedi, J. Perdigues, “Optimization and throughput estimation of optical ground Networks for LEO-downlinks, GEO-feeder links and GEO-relays”, Proceedings of SPIE, 10096. Photonics West, San Francisco, CA, 2017.

[22] A. Biswas, S. Piazzolla, “The Atmospheric Channel”, in “Deep Space Optical Communications”, H. Hemmati, Ed., Wiley-Interscience, 2006

[23] M. Toyoshima, T. Jono, K. Nakagawa, A. Yamamoto, Optimum divergence angle of a Gaussian beam wave in the presence of random jitter in free-space laser communication systems. J. Opt. Soc. Am. 19, 567–571 2002

[24] L. Andrews, R. Phillips, “Laser Beam Propagation through Random Media”, SPIE Press, 2005

[25] D. Giggenbach, F. Moll, “Scintillation Loss in optical low earth orbit data downlinks with avalanche photodiode receivers,” in 2017 IEEE International Conference on Space Optical Systems and Applications (ICSOS), Naha, Japan, 2017

[26] D. Giggenbach, H. Henniger, “Fading-loss assessment in atmospheric free-space optical communication links with on-off keying", Optical Engineering 47 (4), SPIE - Optical Press, April 2008

[27] D. Giggenbach, A. Shrestha, C. Fuchs, F. Moll, K. Saucke, “Reference Power Vectors for the Optical LEO Downlink Channel”, IEEE-Xplore, International Conference on Space Optical Systems 2019 (ICSOS), Portland, USA, 2019

[28] S. Lambert, W. Casey "Laser Communications in Space", Artech House, p. 149ff, 1995

[29] D. Rollins, J. Baars, D. Bajorins, et al “Background light environment for free-space optical terrestrial communications links”, Proc. SPIE 4873, Optical Wireless Communications V, 2002

[30] E. Bell, et al, "Spectral-Radiance of Sky and Terrain at Wavelengths between 1 and 20 Microns. II. Sky Measurements", JOSA Vol. 50, Dec. 1960

[31] ITU-R P.1621-2, “Propagation data required for the design of Earth-space systems operating between 20THz and 375THz”, International Telecommunication Union – Radiocommunication Sector, 2015

[32] W. R. Leeb, “Degradation of signal to noise ratio in optical free space data links due to background illumination”, Applied Optics, 28, 1989

[33] J. Pacheco-Labrador, A. Shrestha, J. Ramírez Molina, D. Giggenbach, ”Implementation of variable data rates in transceiver for free-space optical LEO to ground link”, SPIE, Environmental Effects on Light Propagation and Adaptive Systems III, 21-25 Sep 2020

[34] D. Caplan, “Laser communication transmitter and receiver design”, J. Opt. Fiber. Commun., 2007, Springer Science

[35] D. Giggenbach, R. Mata-Calvo, Sensitivity Modeling of Binary Optical Receivers”, Applied Optics, Vol. 54, No. 28, October 1, 2015

[36] J. Rothman, P. Bleuet, L. Andre, Q. Abadie, G. Bordot, et al “HgCdTe APDs for free space optical communications”, Proc. SPIE 10524, Free-Space Laser Communication and Atmospheric Propagation XXX, 2018

[37] S. Pers, J. Rothman, P. Bleuet, et al, “Reaching GHz single photon detection rates with HgCdTe avalanche photodiodes detectors”, ICSO 2020, Proc of the SPIE 11852, March/April 2021

[38] R. McIntyre, “Multiplication noise in uniform avalanche diodes”, IEEE Transaction on Electron Devices, Vol. ED-13, no. 1, Jan. 1966

[39] R. McIntyre, “The distribution of gains in uniformly multiplying avalanche photodiodes: Theory,” IEEE Transactions on Electron Devices, vol. 19, no. 6, June 1972

[40] J. Conradi, “The distribution of gains in uniformly multiplying avalanche photodiodes: Experimental,” Electron Devices, IEEE Transactions on, vol. 19, no. 6, p713 – 718, June 1972

[41] P. Webb, R. McIntyre, and J. Conradi, “Properties of avalanche photodiodes”, RCA Review, vol. 35, p. 234–278, 1974.

[42] Application Note, “Avalanche photodiodes – A User Guide”, PerkinElmer Optoelectronics, 2010

[43] Application Note, “Using InGaAs Avalanche Photodiodes”, JDSU Corporation, 2005

[44] J. Huang, “Temperature Dependency Study of Mesa-Type InGaAs/InAlAs Avalanche Photodiode Characteristics”, Hindawi Advances in OptoElectronics, 2017

[45] G. Agrawal, “Fiber-Optic Communication Systems, Third Edition”, John Wiley & Sons, New York, 2002

[46] R. G. Smith, S. D. Personick, “Receiver Design for optical fiber communication systems”, chapter 4 in “Semiconductor Devices for Optical Communications”, H. Kressel, Ed., p89 ff, Springer, New York, 1980

[47] N. Sorensen, R. Gagliardi, ”Performance of Optical Receivers with Avalanche Photodetection”, IEEE Transactions on Communications, Vol. 27, No 9, p 1315-1321 Sept 1979

[48] S. B. Alexander, ”Optical Communication Receiver Design“, SPIE Tutorial Texts Vol. TT22, 1997

[49] S. D. Personick, “Optical Detectors and Receivers”, Journal of Lightwave Technology, Vol. 26, No. 9, 2008

[50] J. C. Campbell, “Recent Advances in Telecommunications Avalanche Photodiodes”, J. of Lightwave Technology, Vol. 25, No. 1, January 2007

similar document has been published as: “Giggenbach, D. Free-Space Optical Data Receivers with Avalanche Detectors for Satellite Downlinks Regarding Background Light. Sensors 2022, 22, 6773. https://doi.org/10.3390/s22186773“

[51] Y. Yamamoto “Fundamentals of noise processes - chapter12: Classical Communication Systems”, Cambridge University Press, 2012
[52] D. Ong, J. Green “Avalanche Photodiodes in High-Speed Receiver Systems”, Photodiodes - World Activities in 2011, Prof. Jeong Woo Park (Ed.), 2011
[53] G. Jacobsen, “Sensitivity Limits for Digital Optical Communication Systems”, J. Opt. Commun. 14-2, 1993
[54] V. Reddy, R. Nerem, S. Woo Nam, R. Mirin, V. Verma, „Superconducting nanowire single-photon detectors with 98% system detection efficiency at 1550 nm”, Vol. 7, No. 12 / December 2020 / Optica, OSA, 2020
[55] D. Green, “Constant-Current APD Bias Method Automatically Optimizes Optical Comms Performance”, Electronics Design 2017
[56] Laser-Components Corporation, “IAG-Series”, Datasheet, 2019
[57] Maxim-Integrated Corporation, “MAX3658 - 622Mbps, Low-Noise, High-Gain Transimpedance Preamplifier”, Datasheet, 2007
[58] Tran Van Muoi, “Receiver design for high-speed optical-fiber systems”, J. Lightwave Technol., vol. 2, page 243, 1984

similar document has been published as: “Giggenbach, D. Free-Space Optical Data Receivers with Avalanche Detectors for Satellite Downlinks Regarding Background Light. Sensors 2022, 22, 6773. https://doi.org/10.3390/s22186773“